GEOPHYSICS, VOL. 81, NO. 6 (NOVEMBER-DECEMBER 2016); P. D679–D685, 9 FIGS., 1 TABLE.
10.1190/GEO2015-0376.1

Analysis of outer-casing echoes in simulations of ultrasonic pulse-echo through-tubing logging

Erlend Magnus Viggen[1], Tonni Franke Johansen[1], and Ioan-Alexandru Merciu[2]

ABSTRACT

Cased petroleum wells must be logged to determine the bonding and hydraulic isolation properties of the cement. Ultrasonic logging of single casings has been widely studied and is commercially available. However, ultrasonic logging in multiple-casing geometries is an unexplored topic despite its importance in plug and abandonment operations. Therefore, current logging technologies should be studied to evaluate whether they indicate the potential for multiple-casing logging. In this study, we used two finite-element models of pulse-echo logging. The first model represents logging in the transverse cross section of a double-casing well. The second model is a copy of the first, but with the outer casing and formation removed so that the pulse-echo transducer receives only a resonant first interface echo from the inner casing. By subtracting the received signals of the second model from those of the first, we can recover the third interface echo (TIE) signal representing the resonant reflection from the outer casing. This signal is used to study what information can, in principle, be drawn from TIEs in double-casing geometries, with the caveat that TIEs can only approximately be recovered in practical cases. We simulated variations of the material in the annulus beyond the outer casing, of the thickness of the outer casing, and of the eccentering of the outer casing. We have determined that the first two of these variations have only weak effects on the TIE, but that the eccentering of the outer casing can, in principle, be found using the TIE arrival time.

INTRODUCTION

As the production life of more and more oil fields is coming to an end, plug and abandonment (P&A) operations are gaining more attention from the industry and regulators. In these operations, the well must be hydraulically sealed to permanently avoid leakage. With the increase in the number of P&A operations in the near future, the associated time and cost expenditures are set to increase dramatically. It is therefore very important to look into more efficient P&A methods that still safely ensure permanent sealing.

To avoid the time-consuming and expensive job of removing casings from the well, as many casings as possible should be left in place. For hydraulic isolation to still be ensured, thorough knowledge is required of the preexisting hydraulic barriers, such as cement, in the well at the time of P&A. Cement bond logs are available in some cases, but these may be outdated by several decades, and may have been performed before additional casings were inserted into the well. Thus, new logs must in most cases be made.

However, current logging methods have been developed for single-casing geometries to evaluate, e.g., the casing thickness and the bonding between the casing and the outside material. To use these methods in, e.g., double-casing wells such as the one shown in Figure 1, the inner casings must be removed to gain access to the outer casing. Logging can then be performed in the resulting single-casing system. Instead of performing this time-consuming and costly process, it would be much preferable to use a method that allows logging through multiple casings.

Publications on such multiple-casing logging are scarce, however. We therefore wish to evaluate the possibility of determining information on cement bonding and hydraulic isolation behind multiple casings using current logging technologies. As described in more detail elsewhere (Viggen et al., 2016), we are particularly interested in ultrasonic and sonic technologies because they can provide single-casing logs with high azimuthal resolution. We wish to determine the potential of these technologies, or their lack of it,

Manuscript received by the Editor 13 July 2015; revised manuscript received 7 July 2016; published online 29 September 2016.
[1]SINTEF Information and Communication Technology, Acoustics Research Centre, Trondheim, Norway. E-mail: erlendmagnus.viggen@sintef.no; tonni.f.johansen@sintef.no.
[2]Statoil ASA, Research and Technology, Rotvoll, Norway. E-mail: iom@statoil.com.

for multiple-casing logging. To do so, we will start by studying the simplest cases possible to study what can be achieved in principle with a given method. There is little point in proceeding with more complex and realistic cases, if a given technology does not show potential in these more straightforward scenarios.

In this paper, we look at ultrasonic pulse-echo well logging, in which a rotating transducer is dragged through the inner casing and ultrasonic pulses are shot from the transducer onto the casing at normal incidence. From the reflected signals recorded by the transducer, the thickness of the inner casing (which is affected by corrosion) and the bonded material outside can be estimated (see, e.g., Havira, 1981, 1986; Hayman et al., 1991, 1998; Wright, 1993; Wang et al., 2016).

The simplest multiple-casing logging case that we will examine in this paper is that of through-tubing logging, with water between the two casings shown in Figure 1. We choose these casings not to be corroded or ovalized. Additionally, we choose the transducer to emit a well-behaved pulse and to be well-centered (i.e., to rotate around the center of the inner casing). The one geometric complication that we investigate is eccentering of the outer casing, where it is no longer centered on the same axis as the inner casing, to determine whether this eccentering can be measured.

The signal received by the transducer consists of multiple reflection components. We use the name first interface echo (FIE) for the pulse reflection from the inner casing and the subsequent casing thickness resonance triggered by the pulse. The wave transmitted through the inner casing is reflected from the interface outside the A-annulus (the annulus outside the inner casing). Part of it is transmitted back through the inner casing again and picked up by the transducer. We call this part the third interface echo (TIE). In single-casing logging, only the FIE is analyzed. As described by Miller and Stanke (1999), the single-casing TIE typically represents an echo from the formation or other interfaces, which can be filtered out to improve the logging results and remove log artifacts, such as galaxy patterns. However, the TIE is also potentially useful in that it may provide information about the system outside the inner casing. In a double-casing geometry with fluid between the two casings, the TIE represents the resonant reflection from the second casing.

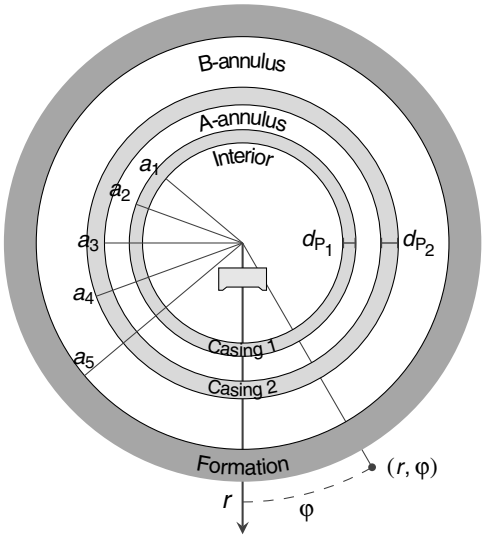

Figure 1. Transverse cross section of the double-casing well geometry and the pulse-echo transducer setup.

In this paper, we test the initial hypothesis that variations of the second casing and variations in the B-annulus beyond the second casing can cause the TIE to vary in a significant and consistent manner. The variations that will be examined in this study are, specifically

- variation of the material in the B-annulus;
- variation of the thickness of casing 2;
- variation of the eccentering of casing 2.

In this study, we used the finite-element method (FEM) to simulate the time-dependent propagation of the ultrasonic pulse in wells. In these simulations, we can extract the TIE signal from the total signal measured by the transducer. This is done through an auxiliary model without a third interface shown in Figure 2b, where the signal measured by the transducer corresponds to the FIE component in the full simulations. This FIE signal can subsequently be subtracted from the received signals in the full simulations to isolate the TIE signal. Thus, the isolated TIE signal represents what could be found from a hypothetical ideal TIE signal processing algorithm, ideal in the sense that it completely removes noise and the FIE signal from the full signal. Practical algorithms, such as the one described by Miller and Stanke (1999) can only asymptotically approach this ideal.

SIMULATION SETUP

Time-domain simulations were performed in a 2D transverse cross section of the full geometry, using the FEM software COMSOL Multiphysics. Although FEM simulations are more time consuming than analytically based modeling (Zeroug, 2000), they are more straightforward because the governing equations of the materials are simulated directly with no approximation except linearity. Furthermore, the FEM simulations do not require a cylindrically symmetric centered geometry unlike the analytically based models (although Zeroug [2004] indicates that it is possible to approximate eccentering in such models as well). The motivation of using this particular software and FEM over other simulation methods is the same as in Viggen et al. (2016), with the additional benefit that the FEM can fit curved geometries well using unstructured meshes, thus avoiding the "staircase approximation" of finite-difference methods.

The simulated cross section is shown in Figure 1. The outer diameter of casing 1 is $2a_2 = 17.78$ cm (7 in.), and its thickness is $a_2 - a_1 = d_{P_1} = 10.36$ mm. For casing 2, its outer diameter is $2a_4 = 24.45$ cm (9⅝ in.), and its thickness is $a_4 - a_3 = d_{P_2} = 13.84$ mm. The borehole diameter is $2a_5 = 32.39$ cm (12¾ in.).

The parameters of the various materials used in the simulation are shown in Table 1. Values of the S-wave speed were not available for some of the solids, and in these cases, c_S was found by an empirical expression from Castagna et al. (1985). Unless otherwise mentioned, the interior and both annuli contained water. A low-reflecting boundary condition, described in COMSOL Multiphysics: Structural mechanics module user's guide (Version 5.2, 2015), was chosen for the outer edge of the system to simulate a semi-infinite formation domain.

In all simulations, the inner casing was kept perfectly centered within the borehole, and the tool axis was kept perfectly centered within the inner casing. The center of these circular structures defines the origin of a polar coordinate system (r, φ) as shown in

Figure 1. When casing 2 is eccentered, it is shifted in the direction of $\varphi = 0^{\circ}$. Due to the mirror symmetry of the eccentered geometry, it was not necessary to simulate transducer orientations outside the interval $\varphi \in [0^{\circ}, 180^{\circ}]$.

The simulated transducer is a 2D cross section of a flat cylindrical transducer. The simulated transducer's face is shielded and slightly concave, with a curvature radius of 20 cm and a width of 25 mm. It is positioned with 44 mm between its face center and the inner casing. The transducer boundaries were modeled in a simple fashion as acoustically hard, as detailed transducer modeling is outside the scope of this work. One side effect of this simplification is that the transducer face is fully reflecting, in contrast to real transducers that are partly absorbing. This causes secondary reflections from the transducer to have unrealistically high amplitudes. In reality, the reflection from the transducer face would reduce the amplitude by an absorption factor, which is strongly dependent on the specific transducer design. However, although these secondary reflections are visible in some of the following figures (specifically, Figures 3 and 7), they do not affect the analysis or conclusions of this paper.

The transducer face transmits an apodized Gaussian pulse into the simulated system by means of an imposed normal acceleration boundary condition

$$\frac{\partial^2 u_n}{\partial t^2} = -B e^{-(t-t_p/2)^2/(2\sigma_t^2)} \sin[2\,\pi f_0 (t - t_p/2)] \sin(s\pi), \quad (1)$$

where $f_0 = 250$ kHz is the center frequency, $t_p = 4/f_0$ is the pulse length, $\sigma_t^2 \approx 4.00\ \mu s^2$ is the time variance for a Gaussian pulse with a relative bandwidth of 0.75, and s is a dimensionless spatial parameter that runs from zero to one over the length of the transducer face. As all the simulated equations are linear, the amplitude B is arbitrary and was chosen as $B = 1\ m/s^2$. The radiation pattern of a transducer can be calculated by its shape and size from expressions found in e.g., Hovem (2012). This particular transducer produces a far-field radiation pattern in which the width of the main lobe, as measured from the angles where its amplitude is −3 dB compared with the axial level, is 16°.

The received signal $S(t)$ is given by a weighted and normalized integral of the pressure p over the transducer face

$$S(t) = \frac{1}{S_0} \int_0^1 p(s,t) \sin(s\pi) ds. \quad (2)$$

The normalization constant S_0 is chosen, such that the FIE amplitude in $S(t)$ is 1. Due to this normalization, the signals $S(t)$ are dimensionless. This approach is in contrast to the more sophisticated approach of some previous publications, such as Zeroug (1998), in which the incident pressure is converted to voltage through a more complex transducer modeling process. However, this complexity would not be necessary or relevant for the analysis in this paper; we are interested in the form of the TIE for a simple and generic double-casing system, not in modeling the output voltage in detail for a specific transducer in this system.

In the auxiliary model, the outer casing was removed and the formation interface was replaced by a radiation boundary condition, as described by COMSOL Multiphysics: Acoustics module user's guide (Version 5.2, 2015). With no reflecting third interface, the received signal contains only the FIE component $S_{FIE}(t)$. This FIE signal can subsequently be subtracted from signals $S(t)$ received in the full model to recover the TIE component $S_{TIE}(t) = S(t) - S_{FIE}(t)$. Both models are shown in Figure 2.

In both models, quadratic triangular elements were used with a maximum size of $dx_{max} = (c_{water}/f_0)/10$, c_{water} being the speed of sound in water. The time step dt was chosen from Courant number considerations so that $c_{P,steel}/(dx_{max}/dt) = 0.4$, $c_{P,steel}$ being the speed of sound in steel. We validated that this resolution is sufficient in a similar study (Viggen et al., 2016).

SIMULATION RESULTS

For our baseline case, the received signal $S(t)$ is shown in Figure 3 along with the FIE signal $S_{FIE}(t)$ from the auxiliary model and the isolated TIE signal $S_{TIE}(t) = S(t) - S_{FIE}(t)$. In this case, the geometry is unaltered and there is water in all annuli. For each signal, an envelope was determined using the Hilbert transform.

In the FIE signal, we see the reflected pulse peak at $t = 68$ μs. It is followed by the decaying casing thickness resonance from which the inner casing thickness and the A-annulus material impedance can be found as explained by Hayman et al. (1991). Subsequent pulses can be seen at $t = 128$ and 188 μs. These pulses have additionally been reflected off the transducer and the inner casing once

Table 1. The P-wave speed c_P, density ρ, P-wave impedance Z, and S-wave speed c_S of simulated materials.

Material	c_P (m/s)	ρ (kg/m^3)	Z (MRayl)	c_S (m/s)
Water	1481	1000	1.48	0
Foam cement	2250	1330	2.99	767
Marls	2400	2200	5.28	897
Class G cement	3700	1800	6.66	2017
Porous and saturated sandstone Formation	3100	2300	7.13	1500
	4645	2200	10.2	2646
Steel casing	5780	7850	45.4	3190

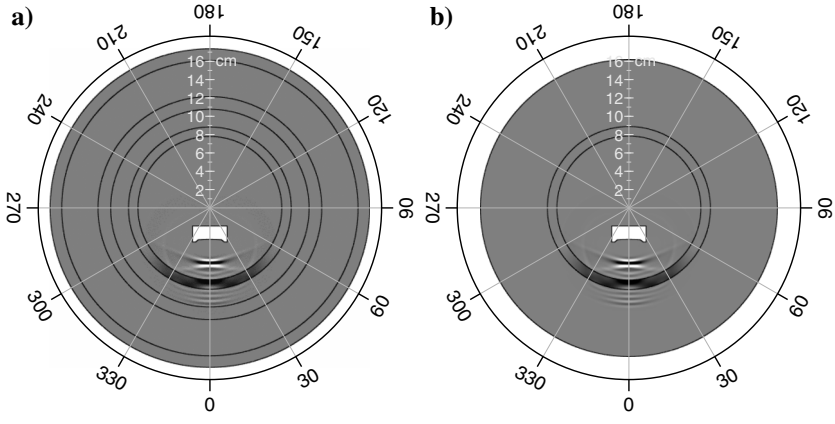

Figure 2. Snapshot of pressure (interior and annuli) and radial displacement (casings) at $t = 50$ μs for (a) the full model and (b) the auxiliary model.

and twice, respectively. As previously mentioned, these reflections are unrealistically strong due to the transducer being modeled as a perfectly reflecting hard surface instead of a partially absorbing one.

The TIE signal starts increasing approximately $t = 93$ μs due to the arrival of the wave, which has been transmitted through the inner casing, reflected from the outer casing, and transmitted back through the inner casing. Its additional traveltime $93 - 68 = 25$ μs matches fairly well with the A-annulus traversal time $2(a_3 - a_2)/c_{\text{water}} = 26.3$ μs. We can spot the TIE signal in the full signal $S(t)$ from approximately $t = 100$ μs. At approximately $t = 119$ μs, we can see an increase in the signal $S_{\text{TIE}}(t)$ due to the wave that has been reflected an additional time between the inner and outer casings before finally being transmitted through the inner casing. Additionally, at approximately $t = 154$ μs, we can see the TIE contribution of the pulse, which has been reflected off the transducer face once, i.e., the pulse we can see at $t = 128$ μs in $S_{\text{FIE}}(t)$. (Because this transducer reflection is unrealistically strong due to the transducer being modeled as an acoustically hard surface, this component of the TIE is correspondingly unrealistically strong in our simulations. More realistically, the strength of this TIE component would depend on an absorption factor determined by the specific transducer design. We will, therefore, not discuss it further in this paper.) The TIE signal may also include a weak echo from the formation, but this is not readily visible in Figure 3.

In the following, we will focus on the first part of the TIE signal because the later parts are typically obscured in $S(t)$ by secondary reflections from the transducer face. For each simulation, we determine the TIE arrival time t_{TIE} as the first time at which the TIE envelope reaches 10% of its maximum value. We additionally determine a representative TIE amplitude as the root-mean-square (rms) value

$$A_{\text{TIE}} = \sqrt{\frac{1}{16\ \mu\text{s}} \int_{0\ \mu\text{s}}^{16\ \mu\text{s}} S(t_{\text{TIE}} + \tau)^2 d\tau}. \tag{3}$$

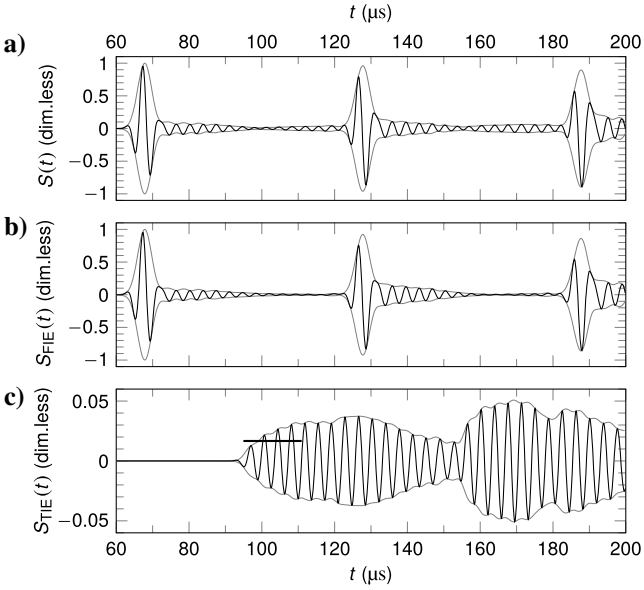

Figure 3. Received signal and its envelope for (a) the full model and (b) the auxiliary model. Both models are shown in Figure 2. (c) The TIE signal found as the difference of the two signals, with a black bar that indicates the representative TIE rms amplitude A_{TIE} (equation 3) and the period over which it was determined.

The integration length of 16 μs corresponds to four periods of the center frequency of the Gaussian pulse in equation 1. This length was chosen to be long enough to give a representative amplitude for the TIE, while being short enough to avoid any significant contribution from the aforementioned multiple reflections of the TIE.

To evaluate the possibility of logging the thickness of the outer casing and the outside bonded material, a series of simulations was performed, one for each combination of five different materials in the B-annulus and three thicknesses d_{P_2} of the outer casing. The resulting values of A_{TIE} against the material impedance Z_B are shown in Figure 4, showing a linear but very weak variation of A_{TIE} with Z_B with different slopes for each thickness d_{P_2}.

From the complete TIE signals with applied Hann windows, the frequency spectra and group delays were also determined and examined. For variations of the B-annulus material, the differences were minor; we could not spot any obvious and consistent variations of the spectra. For variations of the outer casing thickness d_{P_2}, the variations are somewhat larger; three examples are shown in Figure 5.

Another series of simulations was performed to examine the effect of casing 2 eccentering ϵ up to a maximum of $\epsilon = 18.80$ mm.

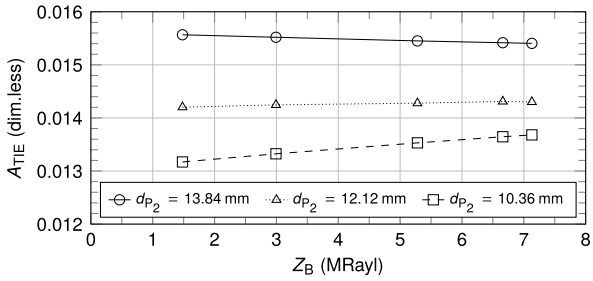

Figure 4. The TIE amplitude against B-annulus impedance Z_B for various outer-casing thicknesses d_{P_2}.

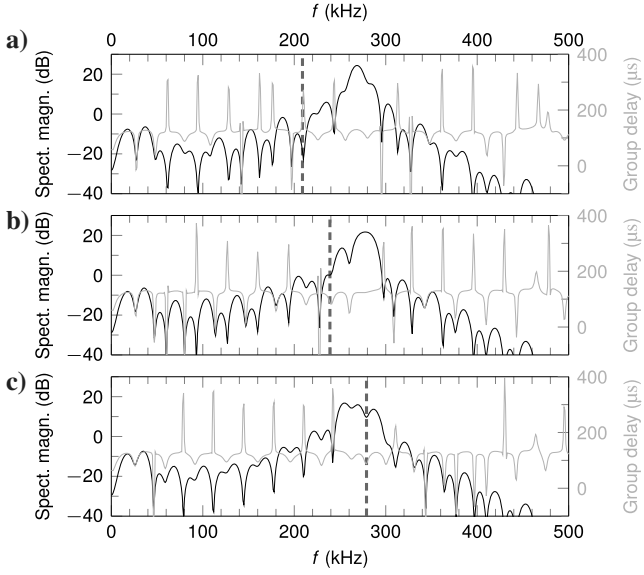

Figure 5. Spectral magnitude and group delay of the TIE signal for $Z_B = 1.41$ MRayl, for (a) $d_{P_2} = 13.84$, (b) $d_{P_2} = 12.12$, and (c) $d_{P_2} = 10.36$ mm. The dashed vertical lines indicate the casing 2 thickness resonance frequencies $f_{P_2} = c_{P,\text{steel}}/(2d_{P_2})$.

For each value of the eccentering, individual simulations were performed for transducer orientations from $\varphi = 0^{\circ}$ to 180° in steps of 30°. Examples of the eccentered models are shown in Figure 6, with examples of the received signals in Figure 7. All simulations were performed with water in the B-annulus.

When the outer casing is eccentered in this way, the third interface distance $a_3'(\epsilon, \varphi)$ deviates from the centered distance $a_3 = a_3'(0, \varphi)$ as

$$a_3'(\epsilon, \varphi) = \epsilon \cos(\varphi) + \sqrt{a_3^2 - \epsilon^2[1 - \cos^2(\varphi)]}. \quad (4)$$

Thus, the additional propagation time of a ray emitted from the transducer to the eccentered third interface and back is

$$\Delta t(\epsilon, \varphi) = \frac{2[a_3'(\epsilon, \varphi) - a_3]}{c_A}, \quad (5)$$

where c_A is the sound speed in the A-annulus.

Figure 8 is based on 29 simulations with various eccenterings and transducer angles. It compares the representative TIE amplitudes A_{TIE} for the different cases. It also compares the difference in TIE arrival times with the predictions of equation 5 for the eccentered and centered cases.

DISCUSSION

Different ultrasonic logging techniques pose different challenges. For pitch-catch techniques, we can see from the received signals shown, e.g., by Zeroug and Froelich (2003), Klieber et al. (2015), and Viggen et al. (2016) that there is typically not a significant overlap between the components corresponding to interaction with the inner casing and those corresponding to interaction with the third interface and beyond. This is in contrast to the pulse-echo technique studied here, where the strong FIE and the weaker TIE components overlap, making them more difficult to separate.

The results of this study must be seen in light of its approach. Using simulations, which are not affected by noise, we are able to recover noise-free TIE signals by subtracting the FIE signal. In real-life cases, practical methods such as the one by Miller and Stanke (1999) cannot completely eliminate the FIE and are still susceptible to some degree to the effects of noise. Therefore, very small variations in the TIE signal may be very difficult to use in real-life cases, because they will be masked by noise as well as imperfections in the practical signal processing algorithms used to isolate the TIEs in the total signal. To investigate the robustness of such algorithms in later work, they could be used to estimate TIEs from simulated transducer signals affected by realistic levels and types of noise.

Additionally, this study neglects several attenuation mechanisms that would weaken the received signals. In practice, the fluids in the interior and the A-annulus would be attenuative, weakening FIE and TIE signal. Also, although our 2D simulations can capture the azimuthal spread of the resonating waves in the casings, they cannot capture the waves' longitudinal spread.

The results in Figure 4 for variation of the annulus impedance show a clear linear trend in A_{TIE} against the impedance Z_B. However, the differences are very small. For $d_{P_2} = 10.36$ mm, the relative difference in signal amplitudes is smaller than 4% between the smallest and largest tested impedances. Such small variations will

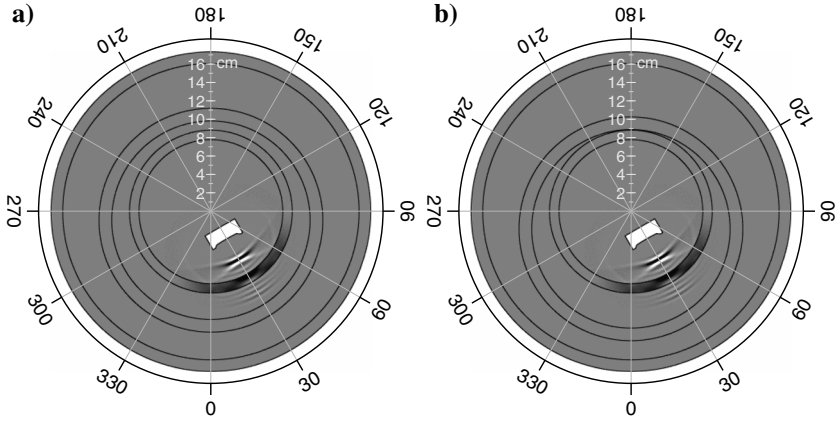

Figure 6. Snapshot as in Figure 2, with casing 2 eccenterings of (a) $\epsilon = 9.40$ and (b) 18.80 mm and a transducer orientation of a 30° angle to the direction of eccentering.

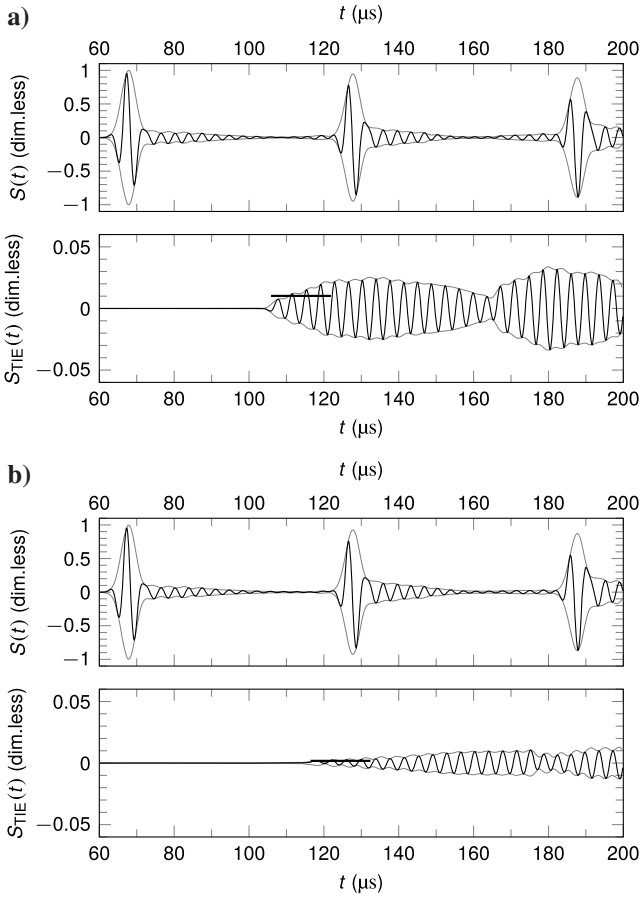

Figure 7. Received full signal and extracted TIE signal from the cases shown in Figure 6 of 30° transducer angle and eccenterings of (a) $\epsilon = 9.40$ and (b) $\epsilon = 18.80$ mm.

be very difficult to detect in practice, indicating that the potential for double-casing bonding logging is low with ultrasonic pitch-catch technology.

The variation of the thickness of casing 2 leads to a greater variation in A_{TIE}. For water in the outer annulus, we have a 15% variation in A_{TIE} between the original geometry ($d_{\mathrm{P}_2} = 13.84$ mm) and the modified geometry with equal casing thickness ($d_{\mathrm{P}_2} = 10.36$ mm). Additionally, we can see that the amplitude of the TIE is reduced when the two casings are of equal thickness. This could be expected, as the two casings have similar thickness resonance frequencies in this case. Thus, the frequencies admitted through the inner casing will to a greater degree also be admitted through the outer casing instead of being reflected back. Consequently, the wave impinging on the third interface is to a lesser degree reflected from the third interface back toward the transducer.

Figure 5 shows that there are visible variations in the spectra for the different values of casing 2 thickness d_{P_2}. However, although we know from Hayman et al. (1991) how to determine the thickness resonances for a single casing from FIE spectra, it is not clear how the thickness resonances for the various outer casings can be determined from the TIE spectra. The casing 2 thickness resonances shown in Figure 5 do not obviously coincide with any extraordinary spectral features that are not also found elsewhere throughout the spectra.

The simulations of varying eccentering showed that the TIE signal nearly disappears for large eccenterings and angles close to $\varphi = 90^{\circ}$. This happens because the wave transmitted through the inner casing hits the outer casing at an oblique angle, so that it is reflected away from the transducer. To shed some light on this, we may use a ray-tracing example. Here, a ray is traced directly forward from the transducer face to the outer casing. With a new direction given by specular reflection at the casing, it is then traced back toward the transducer face. For a given eccentering, the reflected ray will hit the transducer face at some angles, and at some angles it may miss. Figure 9 shows the angles at which the reflected rays would hit and miss the transducer face for several different eccenterings.

However, although the ray-tracing examples give an idea of which cases are more and less problematic, they do not correspond perfectly to more realistic transducer pulses. Rays are a high-frequency approximation, being perfectly narrow and nondiffracting, whereas in reality pulses have a certain physical width. As an example, the disturbance in the A-annulus that is visible in Figure 6 spans almost from $\varphi = 0^{\circ}$ to 60°. Pulse components at wider angles may still be reflected back toward the transducer.

The TIE arrival times shown in Figure 8 are largely as expected from the ray-tracing approximation. However, for the most extreme eccentering, the TIE signal arrives well before the expected time for the angular interval $\varphi \in [60^{\circ}, 120^{\circ}]$. We believe this is due to the aforementioned pulse width effect. Referring to Figure 6b, the outer casing is closer to the transducer face at, e.g., the point $(a_3', 60^{\circ})$ than it is directly in front of the at the transducer at $(a_3', 30^{\circ})$. For transducer angles closer to $\varphi = 90^{\circ}$, the wave impinging on the outer casing will only be reflected back to the transducer from angles where the outer casing is closer.

The TIE arrival times Δt can, therefore, be used to directly determine small eccenterings. For larger eccenterings and transducer angles $\varphi \sim 90^{\circ}$, the TIE amplitude A_{TIE} is lower, and the signal arrives earlier than ray-based theory predicts. Nevertheless, even in the case of full eccentering, the TIE signals at $\varphi = 0^{\circ}$ and 180° are strong and the arrival time is accurate, giving sufficient information to determine the eccentering distance and angle even for very strong eccenterings. Additionally, systematic measured changes in amplitude A_{TIE} with angle can support the determination of the casing eccentering. As shown in Figure 8, relatively high A_{TIE} values coincide with normal incidence on the outer casing.

Casing eccentering may also be measured from pitch-catch measurements (Zeroug and Froelich, 2003; Viggen et al., 2016). The pitch-catch technique has the advantage of the payload signal typically being strong, distinct, and not obscured by another signal (see also Klieber et al., 2015). In contrast, the pulse-echo technique gives a TIE signal that is relatively weak and must be separated from the FIE signal. However, in cases where only pulse-echo measurements are available, it may be useful to estimate the position of the outer casing from the TIE arrival time. Additionally, the pulse-echo eccentering measurements can be useful as a complement to other logging techniques.

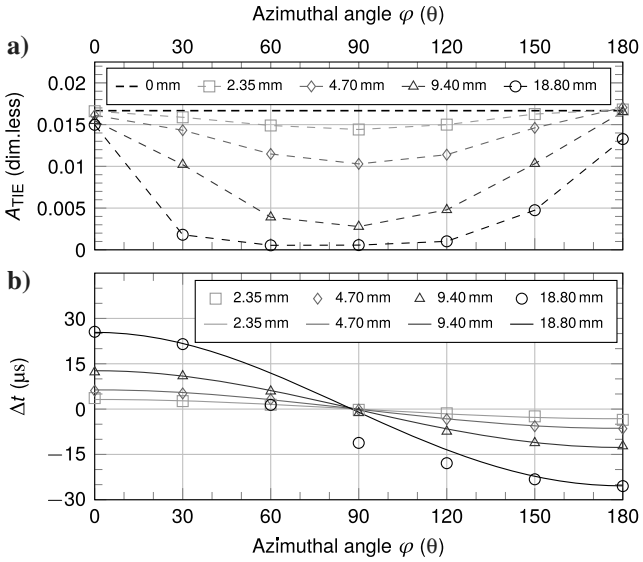

Figure 8. (a) The rms amplitudes of TIE signals as per equation 3 against casing 2 eccentering ϵ and transducer angle φ. (b) Additional TIE propagation time against eccentering and transducer angle, from simulations (marks) and from equation 5 (lines).

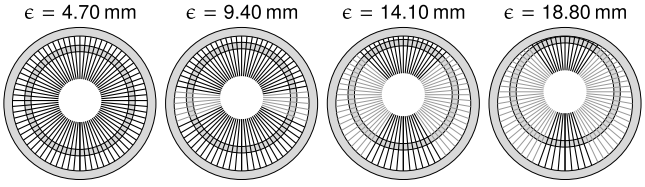

Figure 9. For four different eccenterings, rays are shot from the center of a hypothetical transducer face every 5°. Rays that would hit the transducer face after specular reflection from the outer casing are shown as black and rays that would not are shown as gray.

CONCLUSION

The introduction posed the initial hypothesis that variations of and beyond the second casing can cause significant and consistent variations of the pulse-echo TIE. In this study, we have examined this hypothesis for several specific variations.

When varying the outer annulus' material impedance Z_B and the casing 2 thickness d_{P_2}, the rms value A_{TIE} of the early part of the TIE signal was seen to vary in response. However, these variations were quite weak, and it is therefore unlikely that it will be possible to apply ultrasonic pulse-echo techniques to reliably log the thickness of the outer casing or the material bonded on the outside of the outer casing.

The eccentering of the outer casing was also varied, and it was found that A_{TIE} and the TIE arrival time are dependent on the eccentering distance and the transducer angle. The TIE arrival time in our simulations agreed well with the expected arrival time except at very large eccenterings where the TIE signal is nearly absent for a range of angles. These pulse-echo eccentering measurements can be useful when no other such measurements are available, and as a complement to other logging techniques.

We may posit two final hypotheses. First, that the variations of the TIE with the outer casing thickness and the B-annulus material are too subtle to be reliably used in through-tubing logging. Second, that the TIE arrival time varies significantly and consistently with the eccentering of the outer casing and the transducer angle; even though the TIE nearly disappears at some angles for extreme eccenterings, the eccentering can still be determined from measurements at other angles. It remains to be seen whether the second hypothesis holds in more realistic cases. For logging the thickness of the outer casing and the bonding beyond, the results of this study encourage us to rather look at other options.

ACKNOWLEDGMENTS

This work has been sponsored by Statoil. We are deeply grateful to D. Miller of Miller Applied Science and J. Haldorsen of READ AS. We acknowledge the aid of Statoil's K. Constable and P. Hemmingsen, and we acknowledge the Statoil summer students R. Sivertsen and S. Vik Furuseth for their dedication and constructive feedback.

REFERENCES

Castagna, J. P., M. L. Batzle, and R. L. Eastwood, 1985, Relationships between compressional-wave in elastic silicate rocks and shear-wave velocities: Geophysics, **50**, 571–581, doi: 10.1190/1.1441933.

Havira, R., 1981, Method and apparatus for acoustically investigating a casing and cement bond in a borehole: U.S. Patent 4,255,798.

Havira, R., 1986, Ultrasonic techniques in oil well logging: Proceedings of the IEEE Ultrasonics Symposium, 563–571.

Hayman, A., R. Hutin, and P. Wright, 1991, High-resolution cementation and corrosion imaging by ultrasound: Presented at the SPWLA 32nd Annual Logging Symposium.

Hayman, A. J., P. Parent, P. Cheung, and P. Verges, 1998, Improved borehole imaging by ultrasonics: SPE Production & Facilities, **13**, 5–14, doi: 10.2118/28440-PA.

Hovem, J. M., 2012, Marine acoustics: The physics of sound in underwater environments: Peninsula Publishing.

Klieber, C., T. Brill, S. Catheline, Y. Vincensini, and F. Mege, 2015, Visualization of leaky ultrasonic Lamb wave experiments in multilayer structures: Physics Procedia, **70**, 314–317, doi: 10.1016/j.phpro.2015.08.162.

Miller, D., and F. E. Stanke, 1999, Method of analyzing waveforms: U.S. Patent 5,859,811.

Viggen, E. M., T. F. Johansen, and I.-A. Merciu, 2016, Simulation and modeling of ultrasonic pitch-catch through-tubing logging: Geophysics, **81**, no. 4, D383–D393, doi: 10.1190/geo2015-0251.1.

Wang, H., G. Tao, and X. Shang, 2016, Understanding acoustic methods for cement bond logging: Journal of the Acoustical Society of America, **139**, 2407–2416, doi: 10.1121/1.4947511.

Wright, P., 1993, Method and apparatus for the acoustic investigation of a casing cemented in a borehole: U.S. Patent 5,216,638.

Zeroug, S., 1998, Spectral integral formulae for the response of acoustic transducers in cylindrically curved configurations: IEEE Transactions on Ultrasonics, Ferroelectrics, and Frequency Control, **45**, 768–778, doi: 10.1109/58.677727.

Zeroug, S., 2000, Analytical modeling for fast simulations of ultrasonic measurements on fluid-loaded layered elastic structures: IEEE Transactions on Ultrasonics, Ferroelectrics, and Frequency Control, **47**, 565–574, doi: 10.1109/58.842043.

Zeroug, S., 2004, Forward modeling for ultrasonic leaky Lamb-wave based imaging through a highly contrasting steel cylindrical layer: Proceedings of the IEEE Ultrasonics Symposium, 672–675.

Zeroug, S., and B. Froelich, 2003, Ultrasonic leaky-Lamb wave imaging through a highly contrasting layer: Proceedings of the IEEE Symposium on Ultrasonics, 794–798.